applied sciences

MDPI

Article

Novel Composite Powders with Uniform TiB_2 Nano-Particle Distribution for 3D Printing

Mengxing Chen [1], Xiaopeng Li [2,*], Gang Ji [3], Yi Wu [1], Zhe Chen [1,*], Wouter Baekelant [4], Kim Vanmeensel [5], Haowei Wang [1] and Jean-Pierre Kruth [2]

1 State Key Laboratory of Metal Matrix Composites, Shanghai Jiao Tong University, Shanghai 200240, China; chenmengxing@sjtu.edu.cn (M.C.); eagle51@sjtu.edu.cn (Y.W.); hwwang@sjtu.edu.cn (H.W.)
2 Department of Mechanical Engineering, University of Leuven (KU Leuven), Leuven 3001, Belgium; jean-pierre.kruth@kuleuven.be
3 Unité Matériaux et Transformations, CNRS UMR 8207, Université Lille 1, Villeneuve d'Ascq 59655, France; gang.ji@univ-lille1.fr
4 Department of Chemistry, University of Leuven (KU Leuven), Leuven 3000, Belgium; wouter.baekelant@chem.kuleuven.be
5 Department of Materials Engineering, University of Leuven (KU Leuven), Leuven 3000, Belgium; kim.vanmeensel@mtm.kuleuven.be
* Corresponding author: xiaopeng.li@kuleuven.be (X.L.); zhe.chen@sjtu.edu.cn (Z.C.); Tel.: +32-16-321-212 (X.L.); +86-21-5474-7597 (Z.C.)

Academic Editor: Giorgio Biasiol
Received: 5 January 2017; Accepted: 16 February 2017; Published: 6 March 2017

Abstract: It is reported that the ductility and strength of a metal matrix composite could be concurrently improved if the reinforcing particles were of the size of nanometers and distributed uniformly. In this paper, we revealed that gas atomization solidification could effectively disperse TiB_2 nanoparticles in the Al alloy matrix due to its fast cooling rate and the coherent orientation relationship between TiB_2 particles and α-Al. Besides, nano-TiB_2 led to refined equiaxed grain structures. Furthermore, the composite powders with uniformly embedded nano-TiB_2 showed improved laser absorptivity. The novel composite powders are well suited for selective laser melting.

Keywords: 3D printing; nanocomposites; powders; laser absorptivity

1. Introduction

In the last decade, powder-based additive manufacturing (AM) techniques, such as selective laser melting (SLM), and their applications have evolved significantly. Thus, more and more efforts have been made to develop novel specialized powders, especially in the field of metal matrix composite powders. In general, micrometer-sized ceramic particles are integrated into a metal matrix with the aim of enhancing mechanical properties such as the Young's modulus and strength, while they often severely degrade the plasticity and machinability of the matrix. The ductility and toughness of such metal matrix composites (MMCs) can be maintained or even improved with a simultaneous increase in strength by reducing the particle size to the nanometer range [1,2], hence the so-called nanocomposites. However, to homogeneously distribute nanoparticles in the metal matrix is still a challenging task [3,4]. For example, during powder metallurgy processing, only a low volume fraction of nanoparticles can be dispersed well in a metal matrix under optimized conditions. However, when the volume fraction of nanoparticles exceeds 2 vol. %, the dispersion is worse even after high-energy ball milling for a long time. The nanoparticles tend to agglomerate along the grain boundaries [4].

Titanium diboride (TiB_2) is an attractive candidate as a reinforcement in the Al matrix since it exhibits a high melting point (3173 K), high modulus (565 GPa), high hardness (2500 HV), and

good thermal stability. One of the advantages of these particles is that they have a well-documented crystallographic orientation relationship [5,6] which provides high coherency, thus (1) acting as a nucleus during the solidification of Al [5]; and (2) lowering the solid-particle interfacial energy to improve particle engulfment during solidification [6]. Besides, previous works have proved that the rapid solidification process and the decrease of the particle size can improve the particle engulfment during solidification [7–10].

Here we show that a uniform distribution of a high fraction of TiB_2 nanoparticles in Al-based metal matrix powders was achieved by gas atomization solidification processing through the combined effects of coherency among the metal-diboride interface, supercooling and a nanoscale particle size. The resulting Al-based composite powders exhibited a fine grain structure, with uniformly dispersed TiB_2 nanoparticles, and thereby are promising candidates for nanocomposite synthesis. Since one of the major challenges in the laser-based additive manufacturing (AM) field (e.g., selective laser melting) is the severe limitation of powder materials with acceptable laser processability [11–13], the introduction of pre-embedded nanometer-sized TiB_2 into the metal matrix (e.g., Al-Cu-Mg in this study) would help to expand the powder materials' palette for AM due to the higher laser absorptivity of TiB_2 compared to the Al matrix [14]. Furthermore, since the nanometer-sized TiB_2 particles are embedded into spherical, micrometer-sized composite powders obtained by gas atomization, the powder flowability is not jeopardized.

2. Experimental Procedures

In a previous study, the nanometer sized TiB_2 reinforced Al composites were synthesized via an in-situ reaction process. The size of the in-situ synthesized particles ranged from 20 to 500 nm, but with a predominant number of nanometer sized particles (less than 100 nm) [15]. In the present study, Pure Al was melted at 900 °C with electrical resistance furnace under the protection of an argon atmosphere. The mixed salts of K_2TiF_6 and KBF_4 according to an atomic ratio of Ti/2B were preheated at 250 °C for 2 h and were introduced into the molten aluminum in 15 min. Mechanical stirring of 600 rpm was carried out and heating was maintained at 900 °C for 30 min to allow the in situ TiB_2 particulates to form in the matrix. The reaction slag was skimmed from the surface of the melt. Mg and Al-10Cu master alloys were subsequently added into the melt and homogenized for 10 min. Afterwards, the composite powders were produced by conventional gas atomization. Atomization of the Al-Cu-Mg composite melt was carried out in a confined nozzle atomizer. A schematic diagram of a gas atomization unit and the facility used in the work are shown in Figure 1a,b, respectively. The capacity of the facility used in this experiment is 25 kg melt for a single charging. Prior to melting and atomization, both the melting and the cooling chambers were evacuated to 10^{-2} Pa several times, each time being back filled with nitrogen. During heating of the alloy, its temperature is acquired by means of a thermocouple in the melt. The atomization temperature is 800 °C with a gas pressure of 2.8 MPa. The atomized powder was allowed to cool down to room temperature in the nitrogen gas atmosphere of the atomizer. Afterward, the powders were collected in air. The chemical composition of the composite powders was 3.8 wt. % Cu, 1.3 wt. % Mg and 7.6 wt. % TiB_2 particles with Al balance (a prototype of a 2024 Al alloy with TiB_2 addition), measured by inductively coupled plasma atomic emission spectroscopy analysis (ICP-AES). The powder size distribution was measured by Mastersizer 2000 analyzer. In order to study its microstructure, the as-synthesized powder was sieved into four different size ranges: 63–75 μm (group A); 45–53 μm (group B); 10–26 μm (group C); ≤10 μm (group D). The microstructure of the different gas atomized TiB_2/Al composite powder fractions as well as the distribution of TiB_2 particles was investigated by scanning electron microscopy (SEM), energy dispersive X-ray (EDX) and electron backscattered scattering detection (EBSD). EBSD samples were prepared by Focused Ion beam (FIB) in order to detect both the TiB_2 and Al phase. The crystal structure was characterized by synchrotron radiation X-ray diffraction at the beamline BL14B1 of the Shanghai Synchrotron Radiation Facility (SSRF) using a diffractometer of negligible instrumental

broadening (less than 0.001°), equipped with a double crystal monochromator and a position sensitive point detector. The wavelength of the X-ray used was 0.124 nm.

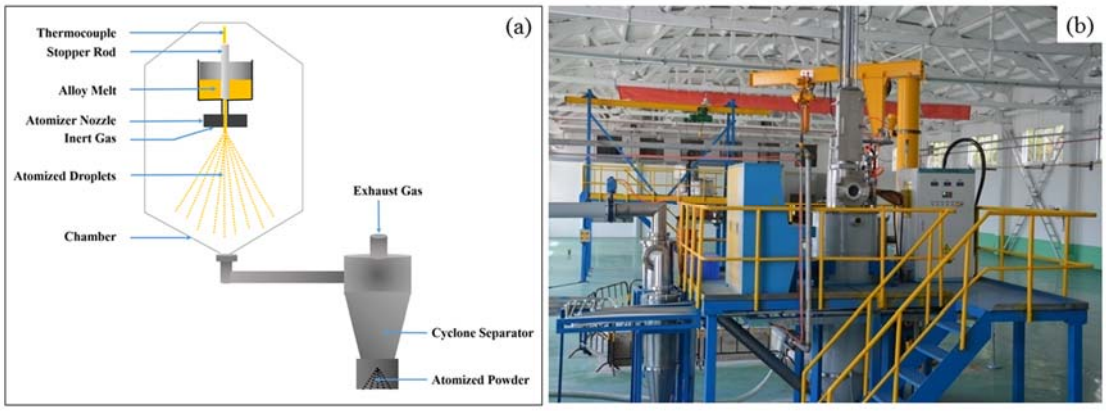

Figure 1. (**a**) Schematic drawing describing the principal of gas atomization technique and (**b**) set-up of the facility used in this work.

Diffuse reflectance spectroscopy (DRS) was measured from 200–2500 nm using an UV-Visible-NIR Lambda 950 Perkin Elmer spectrometer equipped with a 150 mm diameter integrating sphere coated with Spectralon with 1 nm spectral resolution. A Spectralon reference was used to measure the 100% reflectance and internal attenuators were used to determine 0% reflectance in order to remove background and noise. The samples were placed in a quartz cuvette, sealed, and mounted on a Teflon sample holder for the DRS measurement. The reflectance spectra were subsequently converted to Kubelka-Munk (K-M) to calculate the absorption spectra of the powder. This conversion is performed by the device software, using the K-M equation: $f(R) = \frac{(1-R)^2}{2R}$, where R is reflectivity.

3. Results and Discussion

As shown in Figure 2a, the largest Al–3.8Cu–1.3Mg composite powder particles are around 70 μm. All the powders have a spherical morphology. Figure 2b shows the size distribution of the composite powders measured by laser diffraction and the average powder size is 3.68 μm. The atomized composite powders exhibited a typical rapid solidification microstructure with a fine equiaxed grain structure, as shown in Figure 2(c1–f1). The grain size of the different powder fractions was measured from SEM images (more than 1000 grains were measured for each fraction), and the statistical results are illustrated in Figure 2(c2–f2). The equiaxed grain structure had a median grain size of 2.88 μm in fraction A, and then decreased with the decrease of the powder size to 0.81 μm in group D. Figure 2g shows the variation of the average grain size versus the powder size. The grain size decreased as the powder size decreased. Hong et al. [10,16] proved that the average grain size depends linearly on the powder size and is proportional to the cooling rate of the powders. The fine structure of the powders benefits from the high rate of solidification of the gas atomization process, in which the crystallization process has been suppressed due to the large under-cooling. TiB_2 particles distributed both inside the α-Al grains and along the grain boundaries, as indicated by the arrows in Figure 2(e1,f1).

Figure 3a shows a synchrotron X-ray diffraction pattern of TiB_2-reinforced Al–3.8Cu–1.3Mg composite powders. The diffraction peaks of Al, TiB_2 and Al_2Cu were detected correspondingly, as shown in Figure 3a. From the diffraction pattern, the calculated value (7.1 wt. %) of the TiB_2 mass fraction was obtained through the reference intensity ratio (RIR) method [17], which is in agreement with the ICP result. Figure 3b shows the modified Williamson-Hall plot [18] obtained from the diffraction peaks of aluminum. The intercept of the plot indicates that the average grain size was 731.7 nm while the weighted average grain size calculated from the raw data of Figure 2b,g was 870 nm. The difference is due to the fact that synchrotron X-ray diffraction is more sensitive to low-angle grain boundaries,

while the SEM can only show relatively high-angle grain boundaries. It suggests small-angle grain boundaries exist in the composite powders, which was later observed in the EBSD.

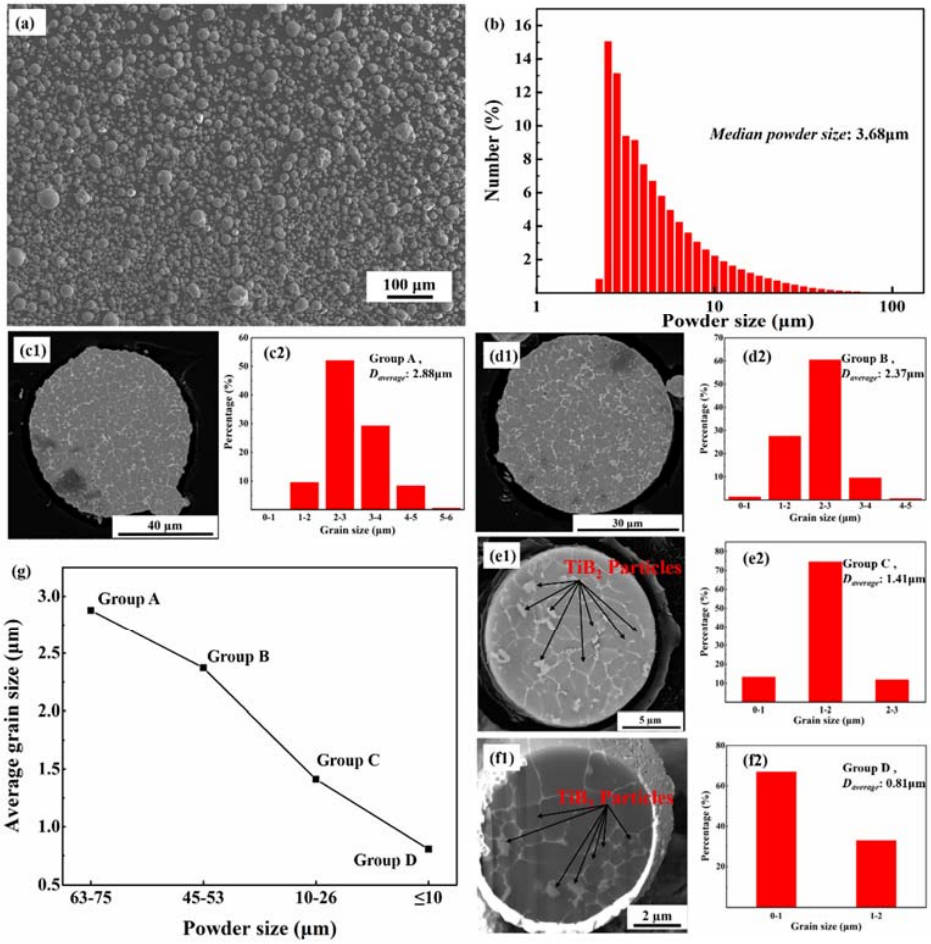

Figure 2. SEM morphology (**a**) and powder size distribution (**b**) of the atomized TiB_2-reinforced Al–3.8Cu–1.3Mg composite powder; SEM micrograph and corresponding grain size distribution of the atomized TiB_2-reinforced Al–3.8Cu–1.3Mg composite powder: (**c1**,**c2**) group A: 63–75 μm; (**d1**,**d2**) group B: 45–53 μm; (**e1**,**e2**) group C: 10–26 μm; and (**f1**,**f2**) group D: ≤10 μm; (**g**) Variation of average grain size with powder size.

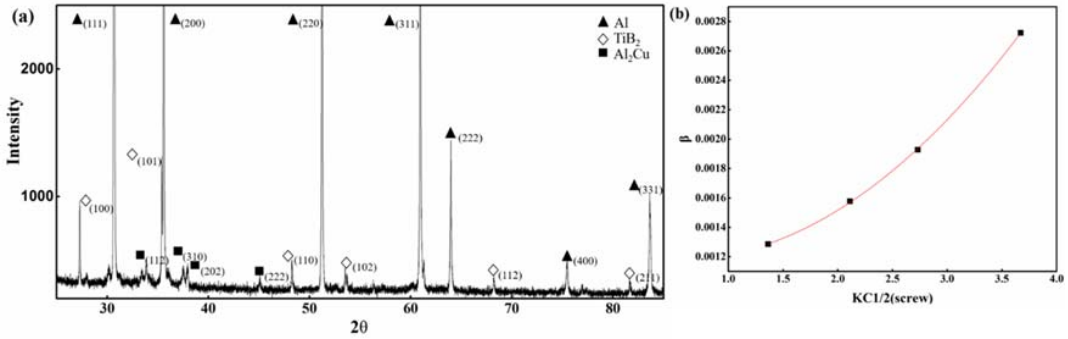

Figure 3. (**a**) Synchrotron X-ray diffraction patterns of the TiB_2-reinforced Al–3.8Cu–1.3Mg composite powder; (**b**) Modified Williamson-Hall plot.

It is pointed out in [19] that along with the decreasing powder size, the rapid solidification microstructure can change from dendritic grains to cellular and even to equiaxed grains. In a recent

study, Zheng et al. [14] investigated atomized Al–Cu–Mg (grade 2024) alloy powders, which exhibit a large dendrite structure. In the current study, the composite powders had a much finer equiaxed grain structure (Figure 2(c1–f1)). The modification of the grain structure was due to the effect of TiB_2 nanoparticles on the solidification process, since TiB_2 particles can significantly improve the crystal nucleation rate of α-Al to refine the grains due to the interfacial effect reported in [5,20].

The powders with typical particle sizes of 50 and 10 μm, respectively, were analyzed by EBSD, applying a fine scan with a 0.1 μm step size. Figure 4a shows an example of an EBSD IPF map of the 50 μm composite powder with TiB_2 phase particles in black contrast. It shows that the micrometer-sized equiaxed grains exhibited random orientations. Figure 4b shows EDS mapping of the elemental distribution of titanium of the same powder, which evidences the homogeneous particle dispersion. In conventional solidification microstructures obtained by casting [6,21], the majority of TiB_2 particles are clustered at the grain boundaries among the equiaxed α-Al grains. In the case of the gas-atomized powders, however, SEM observation shows that TiB_2 particles (indicated by arrows) were distributed both within the grain and along the grain boundaries (as shown in Figures 2(c1–f1) and 4). According to [9,22], the particles are engulfed when the moving front is above the critical velocity. The improved distribution of TiB_2 particles is obtained thanks to the high cooling rate, which promotes the velocity of the advancing solidification front. Furthermore, the transition between particle pushing and engulfment is mainly determined by the interfacial energies between the phases in the system. It has been proven that the TiB_2 particles and the α-Al grains tend to form a high-coherency orientation relationship between the two atomic structures to reduce the solid-particle interfacial energy [6], which assists the engulfment to ensure the uniform distribution of the TiB_2 particles.

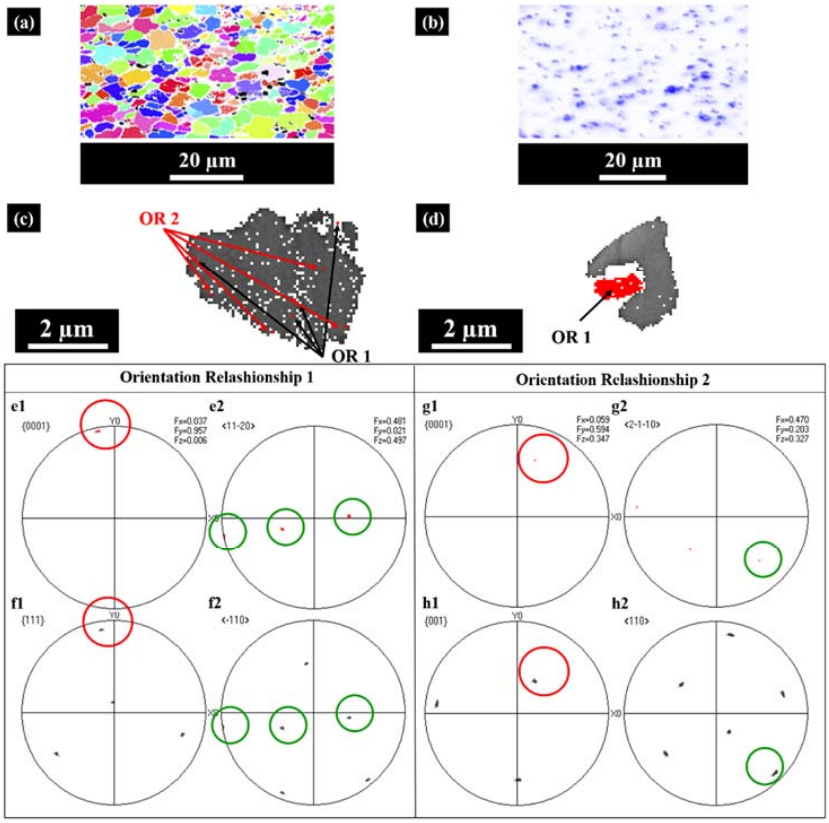

Figure 4. (**a**) EBSD IPF map of a 50 μm composite powder; (**b**) EBSD EDS map of a 50 μm composite powder. Orientation relationships of TiB_2 particles within a grain: (**c**) small particles; (**d**) large particles. (**e1**,**e2**): The {0001} and <11-20> pole figures of certain engulfed TiB_2 particles; (**f1**,**f2**): The {111} and <−110> pole figures of the surrounding aluminum; (**g1**,**g2**): The {0001} and <2-1-10> pole figures of other engulfed TiB_2 particles; (**h1**,**h2**): The {001} and <110> pole figures of the surrounding aluminum.

There are two commonly reported orientation relationships of the nucleation of α-Al on TiB_2 during solidification, noted as OR1 and OR2. OR1 is more commonly encountered according to previous studies [6,23]. Figure 4c,d give an example of small and large particles, respectively, in one grain. It was observed that most TiB_2 particles within one grain have two Euler angles which means that they have two orientation relationships with the surrounding aluminum. OR 1 and OR2 co-exist within one grain, as shown in Figure 4c; Figure 4d shows an example of the big particle with OR1.

Figure 4(e1,e2,f1,f2) present the {0001}<11-20> pole figures of certain engulfed TiB_2 particles and the {111}<−110> pole figures of the surrounding aluminum. The paralleled crystallographic planes and orientations are marked by red and green circles, respectively. The orientation relationship is consistent with OR1:

$(0001)_{TiB2} \| (111)_{Al}$

$[11\text{-}20]_{TiB2} \| [\text{-}110]_{Al}$

Figure 4(g1,g2,h1,h2) present the {0001} <2-1-10> pole figures of other engulfed TiB_2 particles and the {001}<110> pole figures of the surrounding aluminum. The orientation relationship matches with OR2:

$(0001)_{TiB2} \| (001)_{Al}$

$[2\text{-}1\text{-}10]_{TiB2} \| [110]_{Al}$

The statistical analyses of the orientation relationship of recorded TiB_2 particles inside grains and along grain boundaries are summarized in Tables 1 and 2, respectively. Overall, the majority of particles inside the grains (Table 1) form an OR1 relationship with Al as the $[0001]_{TiB2}$ direction is closest to the $[111]_{Al}$ direction [23]. Especially for large-sized TiB_2 particles, OR1 appears more frequently. According to the work by Sen and co-workers [8], the faces of the TiB_2 particles in Al that provide the greatest contact area are the basal faces which form OR1. This enhances the engulfment of particles. It should be noted that three of 34 small TiB_2 particles of the 10 μm powder and four of 13 big particles of the 50 μm powder within the Al grains form neither OR1 nor OR2. This indicates that particle engulfment can take place without a coherent interface in the condition of fast-cooling. However, a well-documented crystallographic orientation relationship can lower the solid-particle interfacial energy to improve particle engulfment during solidification [5]. Most TiB_2 particles segregated at grain boundaries (Table 2) rarely develop any relationship with Al. It is proposed that such a phenomenon mainly results from the restriction of α-Al solid volume fractions (v_{fs}). At the beginning, when the v_{fs} is low, TiB_2 particles are relatively unconstrained and can reorient freely to the growing α-Al in order to reduce the interface energy of TiB_2 and α-Al σ_{SP} by forming OR1 or OR2. As v_{fs} increases, reorientation of TiB_2 becomes increasingly difficult due to the impingement by either neighboring TiB_2 particles or α-Al from multiple directions. Further, during the final stage of solidification, a high v_{fs} along with a high degree of particle-particle interaction will hinder particle motion. Only relatively unconstrained particles will be able to reorient and obtain OR1 or OR2 [6,24]. From the statistical analysis of the orientation relationship, it can be concluded that a uniform dispersion of TiB_2 particles is favored by a coherency interface, supercooling and a nanoscale particle size.

As shown in Figure 5, the composite powder has a reflectivity of ~43% and a corresponding K-M absorption factor of ~0.37 at a wavelength of 1.06 μm, which is typically used for most SLM processes. The K-M absorption factor is comparable to most Al-Si alloy powders between 0.3–0.4. So the laser absorptivity increased significantly due to the addition of TiB_2.

The resulting Al-based composite powders with improved laser absorptivity provide promising candidates for nanocomposite synthesis via AM. The reasons for this are three-fold: (1) the composite powders with higher laser absorptivity will benefit the melt formation during SLM [14]; (2) the introduced nano-sized TiB_2 was pre-embedded mainly into the powder and only a limited proportion was distributed on the powder surface, thus not imposing any negative effect on the flowability of the matrix Al-Cu powder; (3) the interfacial bonding between the nano-sized TiB_2 and the Al-Cu matrix was strong in the gas-atomized composite powder, which can help limit the interface de-bonding during rapid solidification in SLM.

Table 1. Orientation relationship summary of all the recorded TiB_2 particles inside the grain by EBSD.

	Powder Size	Total Number of Recorded Small TiB_2 Particles	Orientation	Number of TiB_2 Particles	Proportion
Small TiB_2 Particles (<200 nm)	50 μm	26	OR1 OR2	24 1	92% 4%
	10 μm	34	OR1 OR2	27 4	79% 12%
	Powder Size	**Total Number of Recorded Big TiB_2 Particles**	**Orientation**	**Number of TiB_2 Particles**	**Proportion**
Big TiB_2 particles (>300 nm)	50 μm	13	OR1 OR2	9 0	69% 0
	10 μm	4	OR1 OR2	3 0	75% 0

Table 2. Orientation relationship summary of all the recorded TiB_2 particles at the grain boundaries by EBSD.

Average Size of TiB_2 Particles	Powder Size	Total Number of Recorded TiB_2 Particles	Orientation	Number of TiB_2 Particles	Proportion
>300 nm	50 μm	17	OR1 OR2	1 0	6% 0
	10 μm	4	OR1 OR2	0 0	0 0

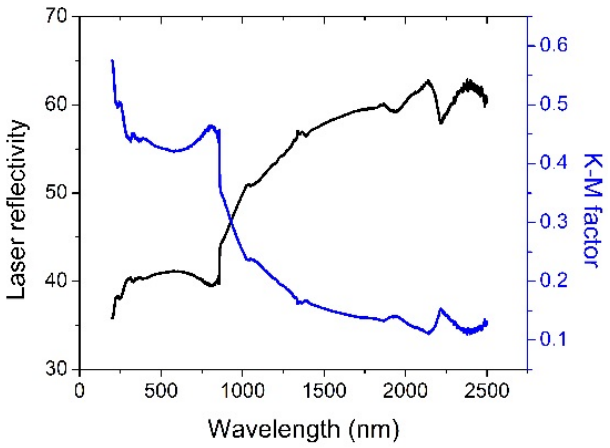

Figure 5. The laser reflectivity and K-M absorption factor of the atomized TiB_2-reinforced Al–3.8Cu–1.3Mg composite powder.

4. Conclusions

Gas-atomized, TiB_2-reinforced Al–3.8Cu–1.3Mg composite powders were synthesized by gas atomization solidification. The composite powders exhibited a fine-grained structure benefiting from the fast cooling condition and the integration of TiB_2 particles, which improved the nucleation rate greatly. The engulfment of TiB_2 particles was achieved, benefiting from the fast cooling rate and the two high-coherency orientation relationships between the particles and α-Al, resulting in a relatively uniform particle distribution in the interior of the grains. The resulting Al-based composite powders with a fine grain structure and uniformly dispersed high-fraction TiB_2 nanoparticles provide promising candidates for nanocomposite synthesis via AM because the TiB_2 pre-embedded nanocomposite powders with improved laser absorptivity largely expand the powder materials palette for AM processes, since the alloy element composition can be easily modified.

Acknowledgments: This work is financially supported by the National Natural Science Foundation of China (Grant No. 51201099 and No. 51301108). Many thanks are also due to the faculty of BL14B beamline at the Shanghai Synchrotron Radiation Facility for their help on synchrotron experiments.

Author Contributions: M.X. Chen and Z. Chen: Co-organized the work, prepared the materials, characterized the materials with SEM, EBSD and Synchrotron X-ray diffraction, wrote the manuscript draft. X.P. Li and W. Baekelant: Materials characterized with laser reflectivity, commented on the manuscript draft. G. Ji: Materials characterized with SEM and TEM analysis, commented on the manuscript draft. Y. Wu: Materials prepared with casting process, commented on the manuscript draft. K. Vanmeensel: commented on the manuscript draft. H.W. Wang and J.P. Kruth: Supervised the materials preparation process, commented on the manuscript draft.

Conflicts of Interest: The authors declare no conflict of interest.

References

1. Liu, G.; Zhang, G.; Jiang, F.; Ding, X.; Sun, Y.; Sun, J.; Ma, E. Nanostructured high-strength molybdenum alloys with unprecedented tensile ductility. *Nat. Mater.* **2013**, *12*, 344–350. [CrossRef] [PubMed]
2. Chen, L.Y.; Xu, J.Q.; Choi, H.; Pozuelo, M.; Ma, X.; Bhowmick, S.; Yang, J.M.; Mathaudhu, S.; Li, X.C. Processing and properties of magnesium containing a dense uniform dispersion of nanoparticles. *Nature* **2015**, *528*, 539–543. [CrossRef] [PubMed]
3. Tjong, S.C. Novel nanoparticle-reinforced metal matrix composites with enhanced mechanical properties. *Adv. Eng. Mater.* **2007**, *9*, 639–652. [CrossRef]
4. Suryanarayana, C.; Al-Aqeeli, N. Mechanically alloyed nanocomposites. *Progr. Mater. Sci.* **2013**, *58*, 383–502. [CrossRef]
5. Fan, Z.; Wang, Y.; Zhang, Y.; Qin, T.; Zhou, X.R.; Thompson, G.E.; Pennycook, T.; Hashimoto, T. Grain refining mechanism in the Al/Al–Ti–B system. *Acta Mater.* **2015**, *84*, 292–304. [CrossRef]
6. Schaffer, P.L.; Miller, D.N.; Dahle, A.K. Crystallography of engulfed and pushed TiB_2 particles in aluminium. *Scr. Mater.* **2007**, *57*, 1129–1132. [CrossRef]
7. Youssef, Y.M.; Dashwood, R.J.; Lee, P.D. Effect of clustering on particle pushing and solidification behaviour in TiB_2 reinforced aluminium PMMCs. *Compos. A Appl. Sci. Manuf.* **2005**, *36*, 747–763. [CrossRef]
8. Sen, S.; Juretzko, F.; Stefanescu, D.M.; Dhindaw, B.K.; Curreri, P.A. In situ observations of interaction between particulate agglomerates and an advancing planar solid/liquid interface: microgravity experiments. *J. Cryst. Growth* **1999**, *204*, 238–242. [CrossRef]
9. Garvin, J.W.; Udaykumar, H.S. Drag on a particle being pushed by a solidification front and its dependence on thermal conductivities. *J. Cryst. Growth* **2004**, *267*, 724–737. [CrossRef]
10. Zheng, B.; Lin, Y.; Zhou, Y.; Lavernia, E.J. Gas Atomization of Amorphous Aluminum Powder: Part II. Experimental Investigation. *Metall. Mater. Trans. B* **2009**, *40*, 995–1004. [CrossRef]
11. Li, X.; Wang, X.; Saunders, M.; Suvorova, A.; Zhang, L.; Liu, Y.; Fang, M.; Huang, Z.; Sercombe, T.B. A selective laser melting and solution heat treatment refined Al–12Si alloy with a controllable ultrafine eutectic microstructure and 25% tensile ductility. *Acta Mater.* **2015**, *95*, 74–82. [CrossRef]
12. Li, X.; Kong, C.; Becker, T.; Sercombe, T. Investigation of Interfacial Reaction Products and Stress Distribution in Selective Laser Melted $Al_{12}Si$/SiC Composite Using Confocal Raman Microscopy *Adv. Eng. Mater.* **2016**, *18*, 1337–1341.
13. Sercombe, T.; Li, X. Selective laser melting of aluminium and aluminium metal matrix composites: Review. *Mater. Technol.* **2016**, *31*, 77–85. [CrossRef]
14. Li, X.P.; Ji, G.; Chen, Z.; Addad, A.; Wu, Y.; Wang, H.W.; Vleugels, J.; Van Humbeeck, J.; Kruth, J.P. Selective laser melting of nano-TiB2 decorated AlSi10Mg alloy with high fracture strength and ductility. *Acta Mater.* **2017**, in press. [CrossRef]
15. Tang, Y.; Chen, Z.; Borbély, A.; Ji, G.; Zhong, S.; Schryvers, D.; Ji, V.; Wang, H. Quantitative study of particle size distribution in an in-situ grown Al–TiB_2 composite by synchrotron X-ray diffraction and electron microscopy. *Mater. Charact.* **2015**, *102*, 131–136. [CrossRef]
16. Hong, S.; Suryanarayana, C.; Chun, B. Size-dependent structure and properties of rapidly solidified aluminum alloy powders. *Scr. Mater.* **2001**, *45*, 1341–1347. [CrossRef]
17. Gualtieri, A.F. Accuracy of XRPD QPA using the combined Rietveld and RIR method. *J. Appl. Crystallogr.* **2000**, *33*, 267–278. [CrossRef]

18. Ungár, T.; Gubicza, J.; Ribárik, G.; Borbély, A. Crystallite size distribution and dislocation structure determined by diffraction profile analysis: Principles and practical application to cubic and hexagonal crystals. *J. Appl. Crystallogr.* **2001**, *34*, 298–310. [CrossRef]
19. Joly, P.; Mehrabian, R. Complex alloy powders produced by different atomization techniques: relationship between heat flow and structure. *J. Mater. Sci.* **1974**, *9*, 1446–1455. [CrossRef]
20. Schneibel, J.H.; Liu, C.T.; Miller, M.K.; Mills, M.J.; Sarosi, P.; Heilmaier, M.; Sturm, D. Ultrafine-grained nanocluster-strengthened alloys with unusually high creep strength. *Scr. Mater.* **2009**, *61*, 793–796. [CrossRef]
21. Chen, F.; Mao, F.; Chen, Z.; Han, J.; Yan, G.; Wang, T.; Cao, Z. Application of synchrotron radiation X-ray computed tomography to investigate the agglomerating behavior of TiB_2 particles in aluminum. *J. Alloys Compd.* **2015**, *622*, 831–836. [CrossRef]
22. Omenyi, S.; Neumann, A. Thermodynamic aspects of particle engulfment by solidifying melts. *J. Appl. Phys.* **1976**, *47*, 3956–3962. [CrossRef]
23. Schumacher, P.; Mckay, B.J. TEM investigation of heterogeneous nucleation mechanisms in Al–Si alloys. *J. Non-Cryst. Solids* **2003**, *317*, 123–128. [CrossRef]
24. Kim, W.; Cantor, B.; Griffith, W.; Jolly, M. TEM characterisation of melt spun Al-3Ti-1B and Al-5Ti-1B alloys. *Int. J. Rapid Solidif.* **1993**, *7*, 245–254.